I&EC research
Industrial & Engineering Chemistry Research

Open Access
This article is licensed under CC-BY 4.0

pubs.acs.org/IECR
Article

Experimental and Computational Fluid Dynamics Studies on Hydrous Hydrazine Decomposition over the $Ir/Ni_{10}Ce$ Catalyst

Panayiota Adamou, Eleana Harkou, Silvio Bellomi, Ilaria Barlocco, Juan Josè Delgado, Xiaowei Chen, Robert Wojcieszak, George Manos, Nikolaos Dimitratos, Alberto Villa,* and Achilleas Constantinou*

Cite This: *Ind. Eng. Chem. Res.* 2025, 64, 8130–8142

Read Online

ACCESS | Metrics & More | Article Recommendations | Supporting Information

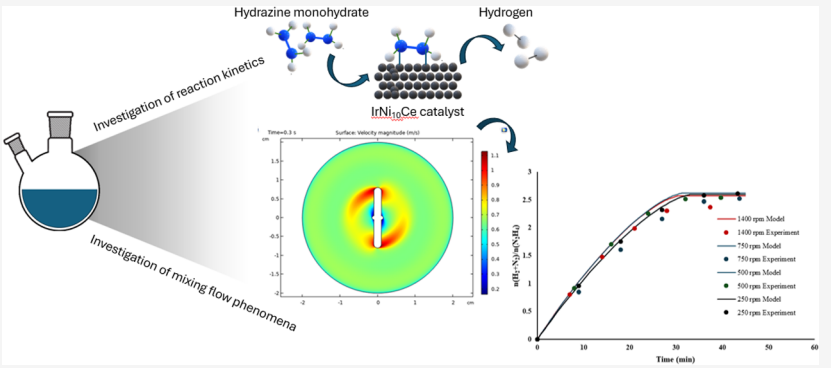

ABSTRACT: Hydrogen storage materials are promising as a fuel source for the adaption of a hydrogen-based economy toward more sustainable energy production. An example of such a material is hydrous hydrazine with a hydrogen content of 8.0 wt %. In this study, an iridium-based catalyst was developed via incipient wetness impregnation and used for hydrous hydrazine decomposition in a batch reactor for H_2 generation. The reaction conditions were optimized in a batch reactor, and the results were validated utilizing computational fluid dynamics (CFD). The developed catalyst achieved a yield of over 80% and a TOF value of around 2400 h^{-1} at 80 °C. Upon validating the experimental data, CFD studies were performed to provide information on the mixing flow phenomena occurring in the reactor. A different batch reactor configuration was developed, which showcased a lower velocity magnitude compared to the original configuration. Models were developed using a one-dimensional (1D) stirrer and four different shapes of two-dimensional (2D) stirrers. The results among simulations using 1D and the 2D pivot ring stirrer did not vary significantly, validating the accuracy of the model. Given the small reactor size, the effect of a different shape was expected to be negligible; however, the smallest stirrer resulted in a poor mixing profile, highlighting the importance of appropriate mixing. The potential of using a packed-bed microreactor was also simulated. The yield reached a maximum value and then decreased due to the continuous generation of ammonia in addition to hydrogen. The outcomes of this study make a significant contribution to the integration of experimental data with CFD on the decomposition of hydrous hydrazine for catalytic green H_2 generation, highlighting how reactor configurations influence reaction performance and providing insights for scalability on H_2 technologies.

1. INTRODUCTION

Hydrogen (H_2) is considered a great energy carrier and not an energy source, meaning that it transports and stores energy in a usable form.[1] When compared to hydrocarbon fuels, hydrogen contains larger energy content by mass, lower energy content by volume, and less energy density and burns faster. A major drawback is that H_2 is highly explosive; thus, the study of safe and effective hydrogen storage materials has gained interest in the past decades for the adaptation of a hydrogen-based economy. These materials need to satisfy all of the requirements for transportation, including pressure and temperature handling, by-product recycling, and volumetric/gravimetric hydrogen capacities.[2]

Hydrous hydrazine ($N_2H_4{\cdot}H_2O$; HH) is an inorganic compound containing two amine groups. Due to its high hydrogen capacity (8.0 wt %), it is a promising hydrogen carrier. As seen in eqs 1 and 2, it can follow two paths of decomposition.[3] In addition to H_2, nitrogen (N_2) and ammonia (NH_3) are also produced. These by-products are not greenhouse gases, and therefore, the decomposition of HH generates green H_2. The overall reaction decomposition can be derived, as shown in eq 3. The completion of the reaction via

Received: January 7, 2025
Revised: April 4, 2025
Accepted: April 7, 2025
Published: April 13, 2025

Downloaded via UNIV OF MILAN on July 30, 2025 at 11:46:50 (UTC).
See https://pubs.acs.org/sharingguidelines for options on how to legitimately share published articles.

ACS Publications
© 2025 The Authors. Published by American Chemical Society

https://doi.org/10.1021/acs.iecr.5c00091
Ind. Eng. Chem. Res. 2025, 64, 8130–8142

either the complete dehydrogenation pathway (eq 1) or the incomplete/undesired dehydrogenation pathway (eq 2) strongly depends on the reaction parameters and the nature of the catalyst.[4−8]

$$N_2H_4 \rightarrow 2H_2 + N_2 \quad (1)$$

$$3N_2H_4 \rightarrow N_2 + 4NH_3 \quad (2)$$

$$3N_2H_4 \rightarrow (6x)H_2 + (1 + 2x)N_2 + 4(1 - x)NH_3 \quad (3)$$

Most reactions on heterogeneous catalysts occur on the catalyst surface, and thus, the key influencing factors are their electronic characteristics and surface structure. In the case of HH, altering the sequence of the N−N bond and N−H bond breakage is the main approach to enhance the hydrogen yield of the reaction.[4,9−12] Generally, only metal catalysts exhibit poor results in terms of H_2 yield. However, bimetallic catalysts such as Ni−M (M = Ir, Pd, Pt, Rh)[5,13−15] or supported monometallic catalysts[8,10,16] showed an improved performance in both terms of catalytic activity and the shift toward the first path, producing H_2.

Singh et al.[17] studied the decomposition of HH on different monometallic systems at 25 °C. Rhodium (Rh) exhibited the best performance of all catalysts. In the case of cobalt (Co), ruthenium (Ru), and iridium (Ir), only 0.5 equiv of gases were released, indicating a yield of around 7%. It was also observed that when the same amount of HH was added after the first run, 0.5 equiv of gases were produced again, indicating that the activity of the catalyst remained unchanged.

It is evident that monometallic Ir enhances the undesired pathway. Based on a DFT study reported by Zhang et al.[18] on Ir(111), it was found that mainly N_2 and NH_3 were produced when HH decomposed. The primary reaction route with comparatively low energy barriers was the generation of NH_2 radicals that attack adsorbed hydrazine molecules or subsequent N_2H_x (x = 1−3) species, capturing H atoms and resulting in the generation of N_2 and NH_3. In another study by Lu et al.[19] on a monometallic Ir(111), HH decomposition preferred to begin with an initial scission of N−N bonds toward an NH_2 intermediate. This step promotes the subsequent dehydrogenation of N_2H_x (x = 1−4) to form NH_3 and N_2. This was observed due to the high activation barriers and reaction energies that are an obstacle to the scission of the N−H bond and the recombination of hydrogen molecules at mild temperatures.

Thus, to enhance the yield, monometallic Ir catalysts must be modified, either with the addition of another metal or a support. Iridium-supported catalysts (Ir/CeO_2) were developed by Bellomi et al.[20] for the decomposition of HH. The catalysts were prepared via the deposition−precipitation (DP) method using different precipitating agents or via sol immobilization. The catalysts synthesized using DP with NaOH and sol immobilization exhibited the best performance, with H_2 yields of 38.9 and 36.6%, respectively. The impact of the support was also examined by employing TiO_2 and NiO, in addition to CeO_2, on particles prepared by sol immobilization. The Ir/NiO catalyst achieved the highest yield toward H_2 (83.9%) and great stability through recycling testing.

As it was mentioned, in addition to the nature of the catalyst, experimental conditions are also critical for the enhancement of the desired reaction pathway. Most of the reported studies were conducted on batch systems, which are very simple. However, despite the simplicity of the reactor systems, conducting real-time experiments trying different parameters to find the optimum is time-consuming, and lots of reagents/products are wasted. Computational fluid dynamics (CFD) can be implemented in this case. With the use of CFD, not only data are predicted and validated but also the whole process can be optimized,[21−24] since CFD can provide information on transport phenomena to understand interactions occurring within the reactor.

In literature, few studies focus on catalytic green H_2 generation using CFD, with most of them focusing on NH_3 decomposition on microchannels or membrane reactors[25−27] and investigating velocity, temperature, and concentration distributions. A study from our group[28] examined HH decomposition on a commercial rhodium catalyst, combining experimental work and CFD studies. Parameters such as stirring rate, temperature, mass of catalyst, and HH and sodium hydroxide (NaOH) concentrations were examined to determine the optimum experimental conditions for H_2 production. Computational studies validated very well all the experimental results, and also CFD studies were conducted to better understand the reactor system. Velocity and temperature fields, as well as the distribution of HH and the catalyst particles, were investigated, and the findings showed how the system's uniformity is affected by different reaction conditions.

An $Ir/Ni_{10}Ce$ catalyst was synthesized via a wet-impregnation method and used for the catalytic decomposition of HH in this study. The formation of Ir−Ni interactions can promote hydrogen generation from N-containing molecules, such as hydrous hydrazine, and thus were chosen for this study. Experimental and CFD studies were both performed for parameter optimization such as temperature, stirring rate, HH-to-catalyst molar ratio, and NaOH and HH concentration. The aim of this work is not only validation through CFD but also optimization of the system. Thus, further studies were conducted with a different reactor configuration and different shapes of the stir bar to observe the mixing flow phenomena occurring in the reactor. Lastly, a packed-bed microreactor was designed theoretically, which was compared with that of the batch system.

2. EXPERIMENTAL METHODOLOGY

2.1. Catalyst Preparation. $NiCeO_x$ composite oxides were prepared by a rate-controlled coprecipitation method with a 1 M Na_2CO_3 solution. In a typical preparation, the nitrate precursors, $Ni(NO_3)_2{\cdot}6H_2O$ and $Ce(NO_3)_3{\cdot}6H_2O$, to achieve a Ni/(Ni+Ce) loading of 10 wt %, were added to the desired volume of Milli-Q water (50 mL/g catalyst). The solution was aged for 30 min under 800 rpm stirring. Na_2CO_3 was added at 2 mL/min with a peristaltic pump until a pH of 8.5 was reached, which was monitored with an online pH electrode. The resulting precipitate was aged at room temperature for 3 h and washed three times with hot distilled water. The obtained precipitate was dried at 100 °C overnight and calcined in static air at 650 °C for 5 h. The desired amount of Ir ($IrCl_3$) was deposited by incipient wetness impregnation to achieve a metal loading of 1 wt %. Finally, both the bare and Ir-doped supports were thermally treated in a vertical tubular furnace in N_2 at 400 °C for 2 h and 10% H_2 at 200 °C for 2 h.

2.2. Catalyst Characterization. XRD patterns were collected on a D8ADVANCE diffractometer (Bruker) using Cu Kα_1 radiation (λ = 1.5406 Å). Data were recorded from 20 to 70° 2θ at a step size of 0.02°/s. High-angle annular dark field scanning transmission electron microscopy (HAADF-

https://doi.org/10.1021/acs.iecr.5c00091
Ind. Eng. Chem. Res. 2025, 64, 8130−8142

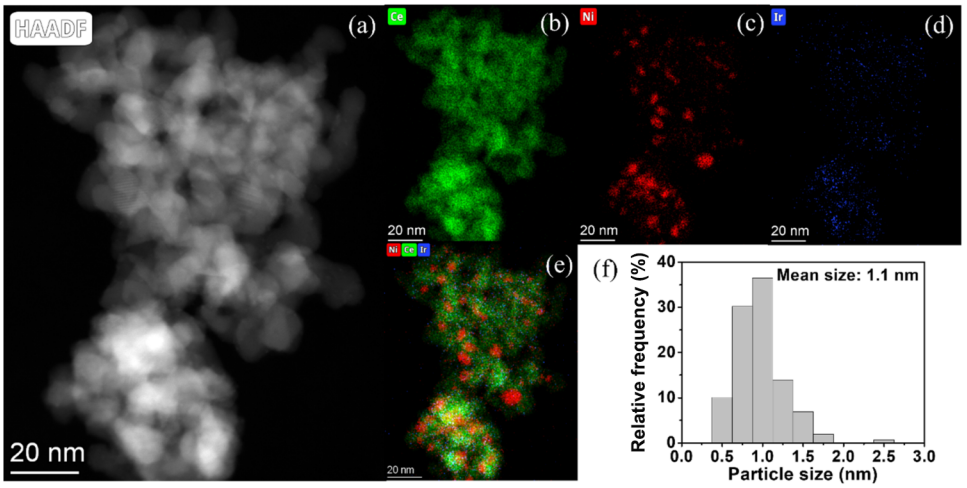

Figure 1. (a) STEM-HAADF image, (b) Ce, (c) Ni, (d) Ir, (e) Ce, Ni, and Ir maps, and (f) particle size distribution of the Ir/Ni_{10}Ce catalyst.

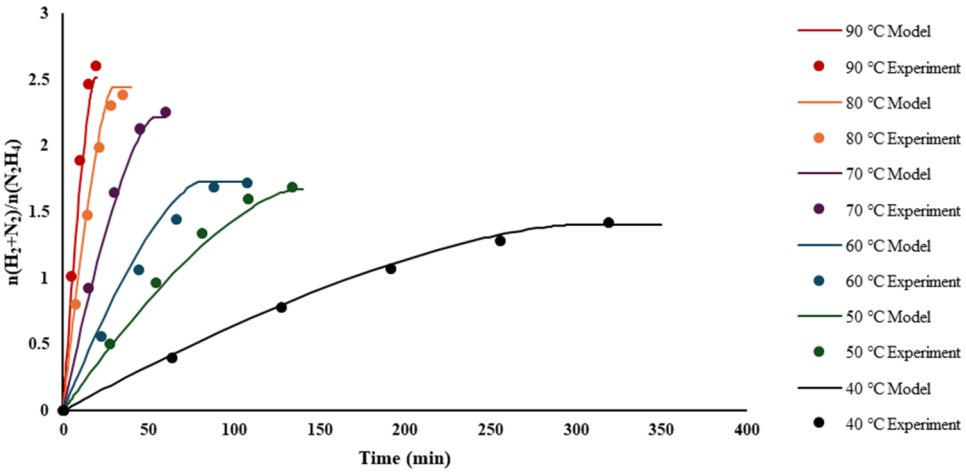

Figure 2. n(H_2 + N_2)/n(N_2H_4) vs time for HH decomposition at temperatures of 40, 50, 60, 70, 80, and 90 °C. Reaction conditions: 150 μL of 3.3 M hydrazine monohydrate, 5 mL of 0.5 M NaOH, stirring rate of 1400 rpm, and 1000:1 substrate-to-metal molar ratio.

STEM) characterization was carried out using a Talos F200X instrument (FEI). The elemental distribution of the samples was analyzed through energy-dispersive X-ray spectroscopy (EDX). EDX mapping was performed with a beam current of 200 ps and a dwell time of 128 μs per pixel to ensure precise resolution. Ir nanoparticles were randomly selected and measured by using ImageJ software. The average particle size (d) was calculated using the following expression: $d = \sum n_i d_i / \sum n_i$, where $n_i \geq 150$. The corresponding metal particle size distributions were also determined. X-ray photoelectron spectroscopy (XPS) analysis of the iridium catalysts was carried out with a Kratos Axis Ultra spectrometer (Kratos Analytical, U.K.). The examined catalysts were irradiated with monochromatic Al Kα radiation (1486.6 eV). Binding energies were referenced to the C 1s peak from the carbon surface deposit at 284.8 eV. The data treatment was performed using CasaXPS Software.

2.3. Catalytic Experiments. The catalytic experiments were conducted on a batch reactor (two-neck round-bottom flask) of 35 mL total volume capacity. The reactor was placed on top of a magnetically stirred hot plate (Figure S1). The catalyst (2.3, 4.7, 9.5, and 19 mg) was added to the reactor with 5 mL of NaOH solution (0−0.5 M) and a magnetic stirrer with the stirring rate ranging from 250 to 1400 rpm. The temperature varied from 40 to 90 °C. After an equilibrium of the system and when the system reached the desired temperature, 150 μL of the HH solution (0.4375−3.3 M) was added to the reactor. The flask was connected to a gas collection system (Man On the Moon X102 kit) to measure the partial pressures of the generated gases as reported in previous studies.[20,28,29] Using the ideal gas law ($pV = nRT$), the pressure measured was quantified by calculating the moles of H_2 and N_2.

These data were then transformed into a dimensionless ratio (λ), λ = n(H_2 + N_2)/n(N_2H_4), between the number of released moles and the initial amount of HH added to the system.

H_2 yield can be obtained by $x = 3\lambda - 1/8$, $1/3 \leq \lambda \leq 3$. A value of 3 indicates no production of NH_3; thus, the yield of H_2 will be 100%.

Turnover frequency (TOF) values were also calculated based on eq 4, assuming all metal particles take part in the reaction. TOF demonstrates the number of products formed per active site per unit time, that is, how fast the catalyst decomposes the reagent.

$$\mathrm{TOF} = \frac{n_{N_2H_4\mathrm{consumed}}}{3n_{\mathrm{metal}}t} \quad (4)$$

https://doi.org/10.1021/acs.iecr.5c00091
Ind. Eng. Chem. Res. 2025, 64, 8130−8142

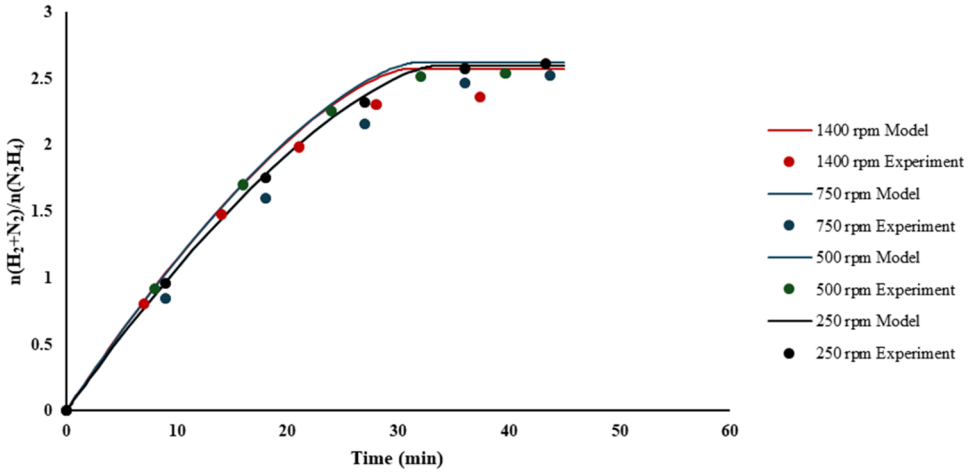

Figure 3. $n(H_2 + N_2)/n(N_2H_4)$ vs time for HH decomposition at stirring rates of 250, 500, 750, and 1400 rpm. Reaction conditions: 150 μL of 3.3 M hydrazine monohydrate, 5 mL of 0.5 M NaOH, 1000:1 substrate-to-metal molar ratio, and 80 °C.

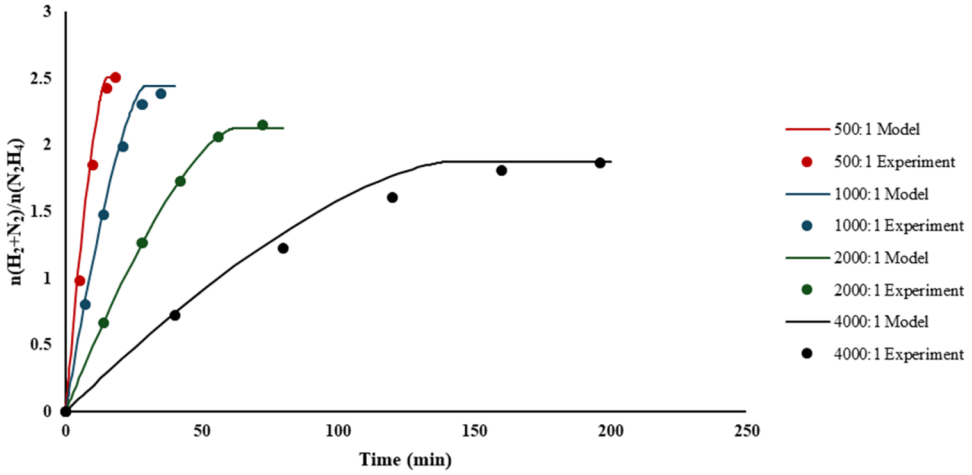

Figure 4. $n(H_2 + N_2)/n(N_2H_4)$ vs time for HH decomposition at the substrate:catalyst molar ratios of 500:1, 1000:1, 2000:1, and 4000:1. Reaction conditions: 150 μL of 3.3 M hydrazine monohydrate, 5 mL of 0.5 M NaOH, 1400 rpm, and 80 °C.

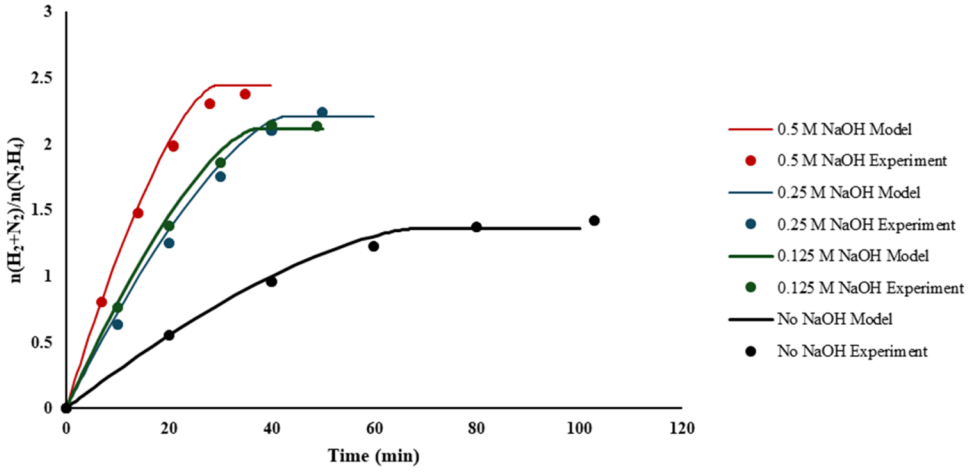

Figure 5. $n(H_2 + N_2)/n(N_2H_4)$ vs time for HH decomposition at NaOH concentrations of 0, 0.125, 0.25, and 0.5 M. Reaction conditions: 150 μL of 3.3 M hydrazine monohydrate, 1000:1 substrate-to catalyst molar ratio, 1400 rpm, and 80 °C.

3. CFD METHODOLOGY

3.1. Reaction Kinetics. For the description of the reaction rate, the power-law model is used as shown below:

$$r = kC_1^{n_1}C_2^{n_2} \quad (5)$$

where r (mol/m^3·s) expresses the rate of reactants; k (1/s) is the specific rate constant; C_1 and C_2 (mol/m^3) indicate the

https://doi.org/10.1021/acs.iecr.5c00091
Ind. Eng. Chem. Res. 2025, 64, 8130−8142

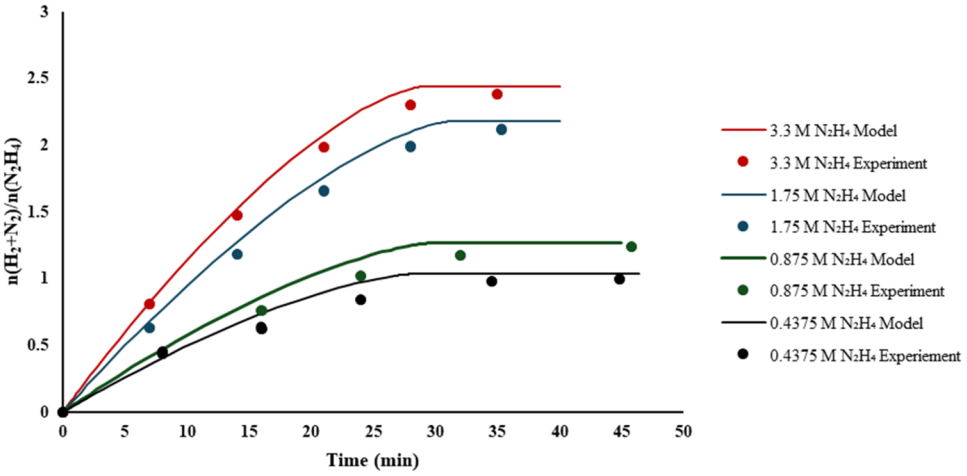

Figure 6. $n(H_2 + N_2)/n(N_2H_4)$ vs time for HH decomposition at HH concentrations of 0.4375, 0.875, 1.75, and 3.3 M. Reaction conditions: 5 mL of 0.5 M NaOH, 1000:1 substrate:catalyst molar ratio, 1400 rpm, and 80 °C.

initial concentration of HH and catalyst, respectively; and n_1 and n_2 are the reaction orders for HH and catalyst, respectively. An activation energy (E_a) of 64.2 kJ/mol was obtained based on the experimental results. An average value of 0.33 was used for the HH reaction order based on a review study.[30] Moreover, based on the experimental results, the order of the reaction toward HH was also calculated with a value of 0.34, close to the one obtained from the literature. For the catalyst concentration, the order value was fixed to 1.00.

3.2. Simulations. COMSOL Multiphysics v6.0 was used in this work, utilizing the Reaction Engineering feature to simulate a 0D model of a batch reactor for the validation of the experimental results. The model consisted of 4 degrees of freedom and 3 s of computational time. The features Heat Transfer in Fluids, Rotating Machinery-Turbulent Flow-k-ε, and Transport of Diluted Species were used for the development of a 2D model, with 6498, 32,486, and 6452 degrees of freedom and 22, 27, and 1 min computational time, respectively. The features Chemistry and Transport of Diluted Species in Porous Media were utilized to simulate a 2D model of a packed-bed microreactor for HH decomposition. The simulation of the packed-bed system had 25,584 degrees of freedom and 7 min of computational time. Details of the equations used in the simulation are presented in the Supporting Information.

4. RESULTS

4.1. Catalyst Characterization. The XRD pattern of the metal oxides (Figure S2) exhibited peaks at 2θ values of 28.3, 32.8, 47.0, 55.7, and 58.4°, which are the characteristic (111), (110), (211), (221), and (220) planes of the cubic CeO_2 structure.[31] On the other hand, no clear reflections of Ni and Ir were detected, probably because Ir and Ni are mostly well dispersed in the CeO_2 support.

The $Ir/Ni_{10}Ce$ catalyst was characterized by TEM, and Figure 1a presents a characteristic STEM-HAADF image. The Ir particles appear small and highly homogeneously distributed, with sizes ranging from 0.5 to 3.0 nm, as shown in Figure 1f. The average particle size was calculated to be 1.1 nm based on the measurement of more than 150 Ir nanoparticles. Although Ni is distributed nearly uniformly with Ce, some Ni agglomeration is observed in certain areas (Figure 1c). The Ce, Ni, and Ir maps in Figure 1e show that Ir does not preferentially localize in Ni-rich regions but is instead dispersed across the entire surface of the $NiCeO_x$ support.

Table S1 summarizes the chemical species observed on the surface and their atomic concentration, as obtained from the survey analysis of the XPS spectra. The results show a low exposure of Ir on the surface (0.24%) and a Ni/Ce ratio of 0.55, higher than the nominal one (0.10), suggesting an enrichment of Ni on the surface of the catalyst. The origin of the high amount of carbon present on the surface (34.93%) is not clear. We assume that it derives from the decomposition of the reactant used during the catalyst synthesis or from the adsorption of CO_2 from the atmosphere. Analyzing the Ir 4f region (Figure S3), we found that Ir is mainly present in the oxidized form.

4.2. Catalytic Decomposition. Catalytic experiments were conducted by varying several parameters (temperature, stirring rate, catalyst mass, and NaOH and HH concentrations), which affect either the reaction yield, catalytic activity, or both. The kinetic profiles of HH decomposition over time were assessed using the normalized ratio (λ) to emphasize the H_2 yield. Subsequently, simulations were then conducted by comparing the experimental values to the predicted values and investigating the robustness of the model. Tables S2 and S3 summarize all of the catalytic performance data. The activities of different monometallic Ir/CeO_2, Ni/CeO_2, and bimetallic $IrNi/CeO_2$ were initially compared. Ni/CeO_2 showed low activity under mild reaction conditions but good selectivity (>95%). On the contrary, Ir/CeO_2 is very active but with low selectivity to H_2 (25%). Bimetallic $IrNi/CeO_2$ catalysts were very active and highly selective. The $Ir/Ni_{10}Ce$ catalyst, which was investigated in this study, was highly selective (89%) probably due to the synergistic effect of Ir and Ni. In particular, the high selectivity can be attributed to the enrichment of Ni on the surface, as evidenced by XPS analysis. After a good validation of the experimental results, CFD optimization studies were performed afterward, focusing mostly on the visualization of the velocity field. A packed-bed microreactor was also simulated for comparison purposes.

4.2.1. Temperature Effect. As reported in many studies, temperature is a crucial parameter that influences the reaction mechanism and, thus, H_2 yield. It is evident in Figure 2 that increasing the temperature increased the yield and the reaction time is severely decreased from 320 min at 40 °C to 19 min at

https://doi.org/10.1021/acs.iecr.5c00091
Ind. Eng. Chem. Res. 2025, 64, 8130−8142

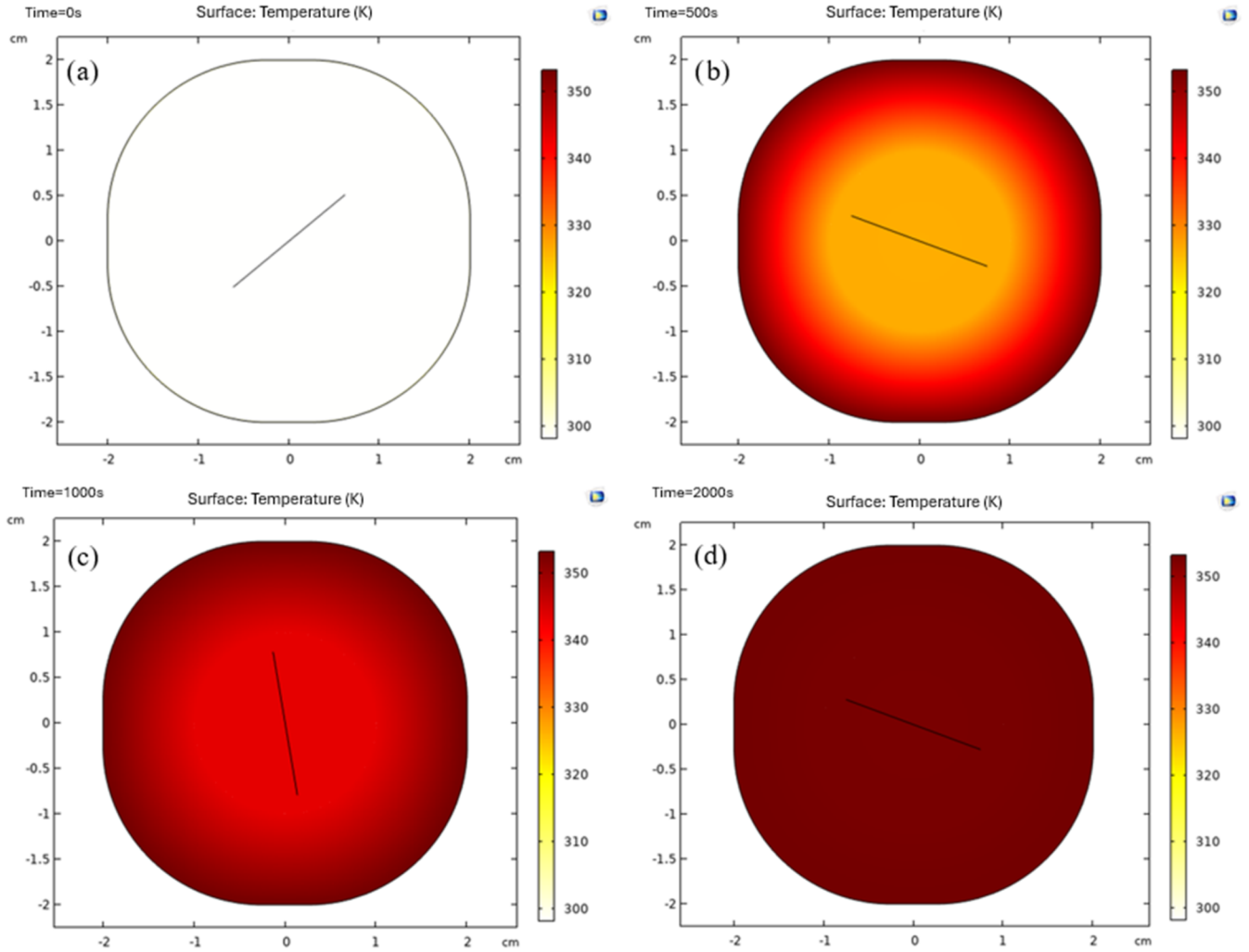

Figure 7. Distribution of temperature (top view of the reactor) at (a) 0 s, (b) 500 s, (c) 1000 s, and (d) 2000 s.

90 °C. Other studies also observed a decreased reaction time.[32−34] However, in our case, it is noticeable that the normalized ratio does not reach the value of 3, meaning that reaction intermediates or NH_3 are also produced. The highest H_2 yield achieved was 89% at 90 °C, and even at this temperature, the catalyst exhibited the best performance. The optimum value chosen for the rest of the experiments was 80 °C, since the difference in the yields was not significant, and in that way, possible deactivation of the catalyst can be avoided. The computational results are in good agreement with the experiments, demonstrating that coupling the power-law model with the kinetic data obtained from the literature and the experimental data, which were used in the simulations, accurately describes the reaction rate of HH decomposition. Observing the TOF values (Figure S4), it is evident that after 70 °C, the TOF values increased rapidly, reaching a value of 4098 h^{-1} at 90 °C. From the Arrhenius plot (Figure S5), an activation energy of 64.2 kJ/mol was calculated.

As reported in a previous study from our group,[28] it is important to examine the temperature distribution in the reactor. A 2D CFD model was developed based on the optimum temperature of 80 °C and a stirring rate of 1400 rpm. A total time of 30 min (Figure S6) is required for the temperature to reach the center of the reactor. Based on our previous study,[28] the time needed for an isothermal temperature distribution seems reasonable, since 25 min were needed to achieve a temperature of 70 °C. Since first an equilibrium run is performed in the system, it is important to ensure that the reactor reaches the desired temperature before adding the solution to the system.

4.2.2. Stirring Rate Effect. Stirring rate is also very important for a reaction's mass transfer limitations. As stated in theory, high velocities decrease the boundary layer between the reactant and the catalytic particle. Thus, it is easier for the reactant species to diffuse from the liquid bulk and be adsorbed on the catalytic surface.[35] The range of values tested was from 250 to 1400 rpm. It is observed from Figure 3 that the yield is not affected by the stirring rate, as expected, and experimental and computational results are in a good agreement with the maximum error of 11% for the stirring rate of 1400 rpm. The TOF values (Figure S7) are within the error of analysis and do not vary much from each other. Thus, the reaction is not affected by diffusion. The optimum value chosen to perform further experiments was 1400 rpm.

The investigation of the uniformity of the system in terms of velocity is also of significant importance, as it affects the distribution of the reactants and the particles and, thus, the chances of collisions for product formation. As it can be seen in Figure S8, due to the high stirring rate in such a small reactor (diameter of 4 cm), at 0.75 s, the velocity magnitude becomes

https://doi.org/10.1021/acs.iecr.5c00091
Ind. Eng. Chem. Res. 2025, 64, 8130−8142

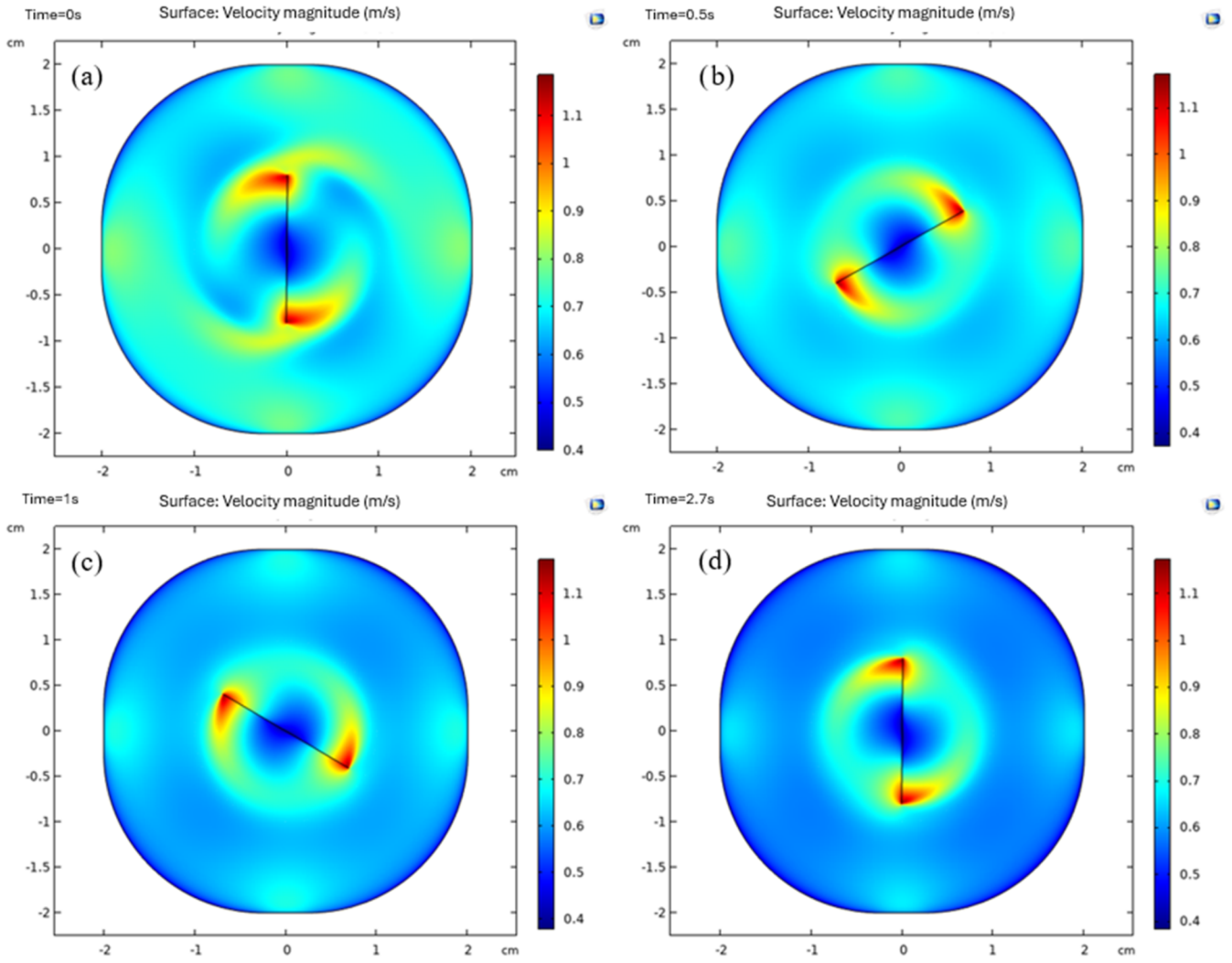

Figure 8. Velocity magnitude (top view of the reactor) at (a) 0 s, (b) 0.5 s, (c) 1 s, and (d) 2.7 s at 1400 rpm.

uniform, as it was also observed in a previous study.[28] Hence, the value of 1400 rpm is the optimum, since it only takes less than 1 s to achieve uniformity.

4.2.3. Catalyst Mass Effect. The amount of catalyst mass can influence both the yield of the reaction and the mass transfer. Thus, different amounts of catalysts of 2.3, 4.7, 9.5, and 19 mg, corresponding to 4000:1, 2000:1, 1000:1, 500:1 substrate-to-catalyst molar ratios, were tested. By increasing the catalyst mass, yield also is increased and reaction time is decreased (Figure 4). The lowest molar ratio resulted in a yield of 60%. This is possible due to the fewer available active sites compared to the higher concentration of the reactant, causing the quick saturation of the active sites, with the available substrate remaining unreacted. The computational simulations are in great agreement with the obtained experimental data. Figure S9 presents the TOF values and the H_2 yield. The 1000:1 molar ratio was chosen as the ideal value, since the difference in the yield results with the 500:1 molar ratio was insignificant and also due to the requirement of higher catalyst mass that could hinder the possibility of performing any further experiments if the 500:1 ratio was utilized.

4.2.4. NaOH Concentration Effect. Many studies regarding the HH decomposition state showed that the addition of alkali media enhances the reaction performance.[7,36−38] This is observed for many reasons. In general, the presence of alkali suppresses the formation of NH_3 and, at a deeper level, accelerates the rate-determining step, which is the breakage of the N−H bond, which acts in favor of producing H_2. Also, due to the ionization of HH in water, the protonated form ($N_2H_5^+$) of HH is formed, leading to the formation of NH_3. However, the presence of alkali suppresses the formation of $N_2H_5^+$. With no NaOH, the yield is 40%, while concentrations above 0.125 M enhance the yield up to 77% (Figure 5), confirming the promoting effect of NaOH. The concentrations of 0.125 and 0.25 M gave similar results in terms of both yield and activity (Figure S10). The experimental results are in good agreement with the computational results. The concentration of 0.5 M was used for the rest of the experiments.

4.2.5. $N_2H_4{\cdot}H_2O$ Effect. The last parameter tested was the concentration of HH. For the previous catalytic tests, a concentration of 3.3 M was used. Therefore, the concentration was halved each time to test lower concentrations. The concentrations of 0.4375 and 0.875 M had yields of 25 and 34%, respectively (Figure 6), and similar TOF values (1535 and 1472 h^{-1}) (Figure S11), while at 1.75 M, there was a "high jumps" in both yield and activity. At 1.75 M, there might be enough substrate compared with the active sites, causing the increase in both yield and TOF. At 3.3 M, the highest yield of

https://doi.org/10.1021/acs.iecr.5c00091
Ind. Eng. Chem. Res. 2025, 64, 8130−8142

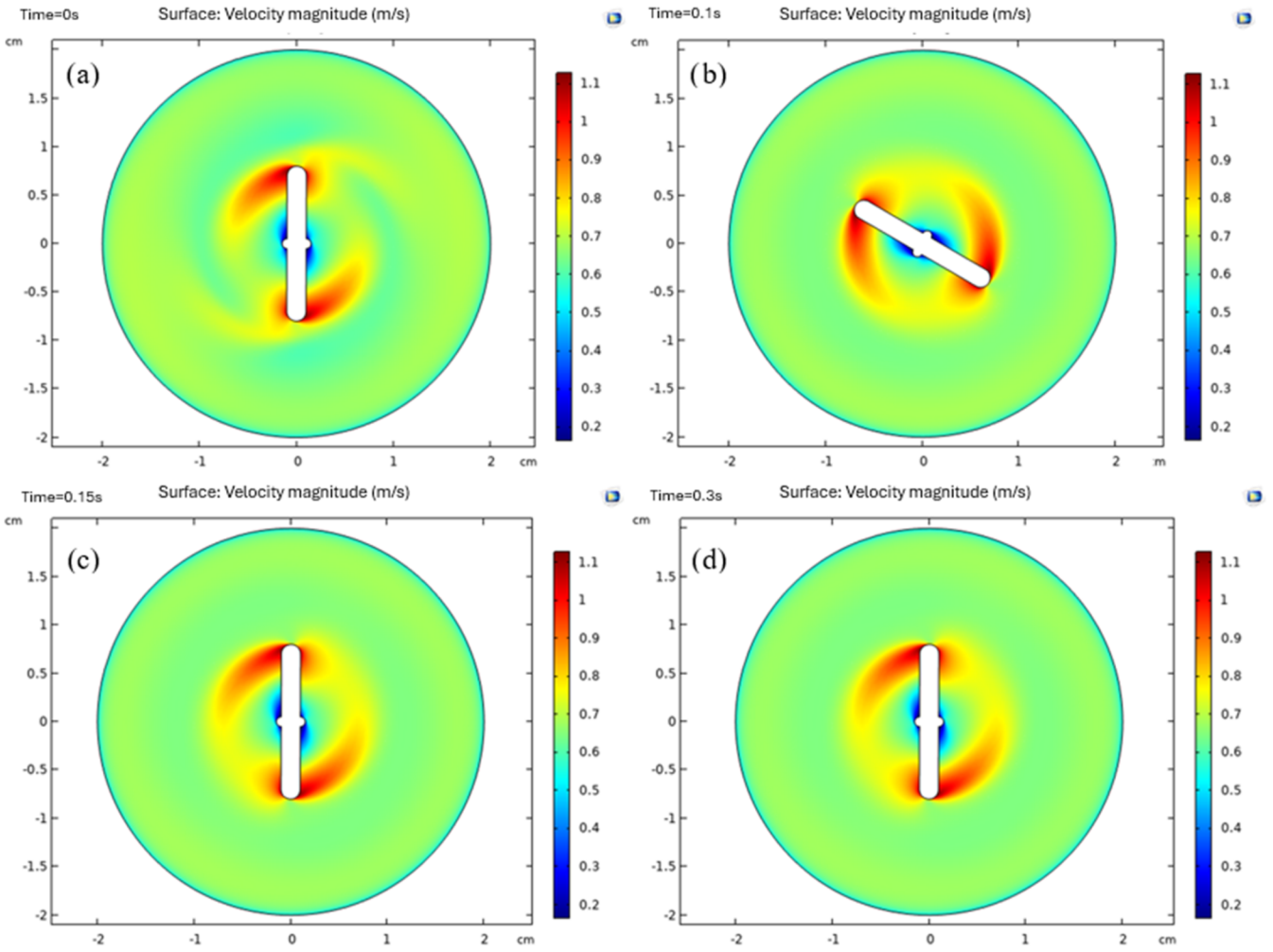

Figure 9. Velocity magnitude (top view of the reactor) at (a) 0 s, (b) 0.1 s, (c) 0.15 s, and (d) 0.30 s at 1400 rpm using a pivot ring stirrer bar.

77% was achieved. The normalized ratio does not reach the maximum value of 3 in any case. This might be the result of the complicated reaction process. Model results are in good agreement with the experimental data. By increasing the concentration of HH above 1.75 M, activity is also increased due to the more available substrate that occupies the catalytic active sites.

The durability of the catalyst over repeated reaction runs is crucial for commercial applications. Therefore, stability tests were performed by using the catalyst without any further treatment (Table S4). The catalyst exhibited remarkable stability after eight repeated cycles, with a slight decrease in the activity observed from the first to the second run. Moreover, an almost constant H_2 selectivity (from 89 to 85%) was observed. The spent Ir/Ni_{10}Ce catalyst after hydrous hydrazine decomposition was characterized using the STEM-HAADF technique. Figure S12a,f shows that the Ir particle size remains small, ranging from 0.5 to 2 nm. The average particle size of the spent catalyst is 1.0 nm, which is very close to that of the fresh catalyst (1.1 nm). Similar to the fresh catalyst, Ni is distributed in isolated islands on the ceria support. However, Ir is not only preferentially located on Ni but also dispersed across the entire Ni_{10}Ce support.

5. OPTIMIZATION

CFD modeling can solve complex equations to interpret mass/heat transport and flow phenomena. In the case of H_2 generation, CFD simulations can optimize reactor design by varying key parameters, ensuring uniform heat and mass transfer distribution and thus enhancing the efficiency of the reaction and yield toward H_2. In that way, reactors will be optimized and then scaled up without needing trial and error in reactor design, cutting costs, and ensuring and providing operational stability.

5.1. Reactor Shape. Laboratory-scale batch systems (round-bottom flasks) are usually used with a total volume capacity of 20−150 mL, with either two or three necks.[4,7,28,30,38−40] For the simulation of the batch reactor, the reactor shape was based on the round-bottom flask that was used in the experiments. In addition to this configuration, there is another flask configuration, which has a flat bottom, and thus its surface is wider and not completely circular. CFD studies were also performed with this geometry to see how it affects the temperature and velocity fields as well as the reactant distribution. For the comparison analysis, the diameter of the reactor was kept the same as that of the round-bottom flask. The temperature distribution is depicted in Figure 7. Compared to the round-bottom flask, where 30 min are needed for the achievement of an isothermal temperature distribution, approximately 33 min are needed in the case of

https://doi.org/10.1021/acs.iecr.5c00091
Ind. Eng. Chem. Res. 2025, 64, 8130−8142

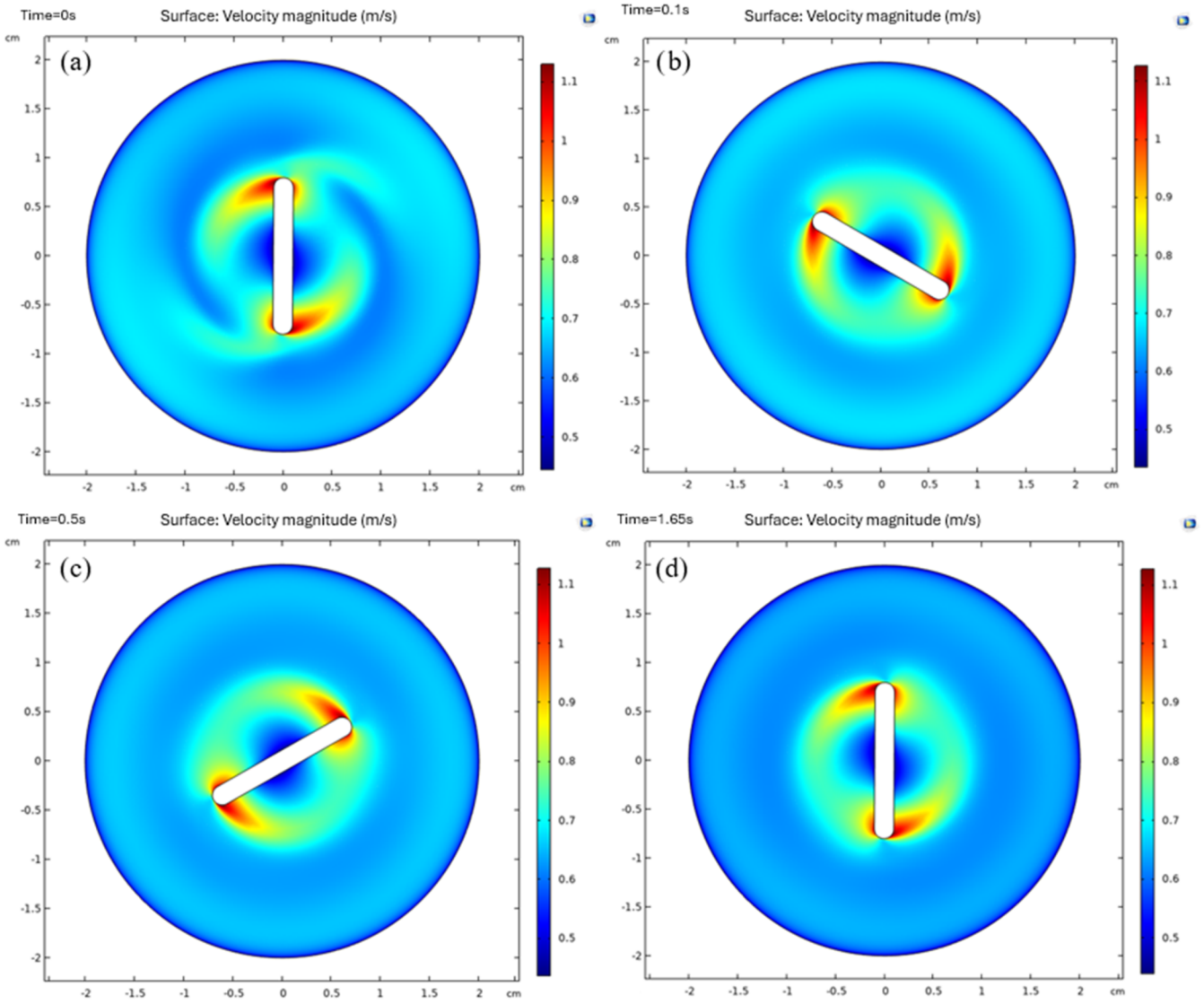

Figure 10. Velocity magnitude (top view of the reactor) at (a) 0 s, (b) 0.1 s, (c) 0.5 s, and (d) 1.65 s at 1400 rpm using a cylindrical bar.

the flat-bottom reactor. The possible explanation behind this slight increase in time is the wider surface area of this reactor, which affects the way the temperature is distributed.

Figure 8 presents the velocity magnitude, and it is evident that even though there is a slight difference between the geometries, this geometry is not so efficient compared to the round-bottom flask. After 2.7 s, the velocity magnitude remains unchanged but not uniform, in contrast to the round-bottom flask. The velocity magnitude is lower (0.5−0.6 m/s) compared to the round-bottom reactor (∼0.67 m/s). Also, dead zones are observed near the reactor wall, pointed with dark blue color and an average velocity magnitude of 0.4 m/s. Thus, in reality, reactant and catalyst particles near this region might be affected by diffusion due to the lower velocity or might be stuck on the reactor wall, unable to participate in the reaction.

The distribution of the HH was also simulated with this reactor geometry. A total time of 1.4 s (Figure S13) is needed for complete distribution through the reactor surface. The slightly increased time, considering the 0.34s needed for the round-bottom flask,[28] is due to the wider surface of the flat-bottom reactor, as it was explained before.

In general, there was a small difference in the temperature and reactant distribution. Only the velocity distribution was significantly different between the two reactors. However, in our case, where a small reactor was used, this difference might not affect the results greatly. Scaling up this process, however, the difference between these two systems will influence both the experimental and the computational results.

5.2. Stirrer Bar Shape. An experiment can be significantly impacted by the choice of the magnetic stirring bar. It is possible to increase the efficiency of mixing as well as enhance the homogeneity. Thus, when selecting a stir bar, there are numerous factors to consider, with the most important being the size and shape. In all CFD cases above, the stirrer was developed as a line segment because it was assumed to be infinitely thin for computational purposes; for example, elements and boundaries are fewer, improving the mesh and the computational time. However, for optimization purposes, the original shape of the stirrer was modeled, as well as other shapes that were available in the laboratory.

5.2.1. Pivot Ring Stirrer Bar. Pivot ring stirrer bars are cylindrical stirrers with a pivot ring at the center of the bar. The purpose of the ring is to maintain the optimum position of

https://doi.org/10.1021/acs.iecr.5c00091
Ind. Eng. Chem. Res. 2025, 64, 8130−8142

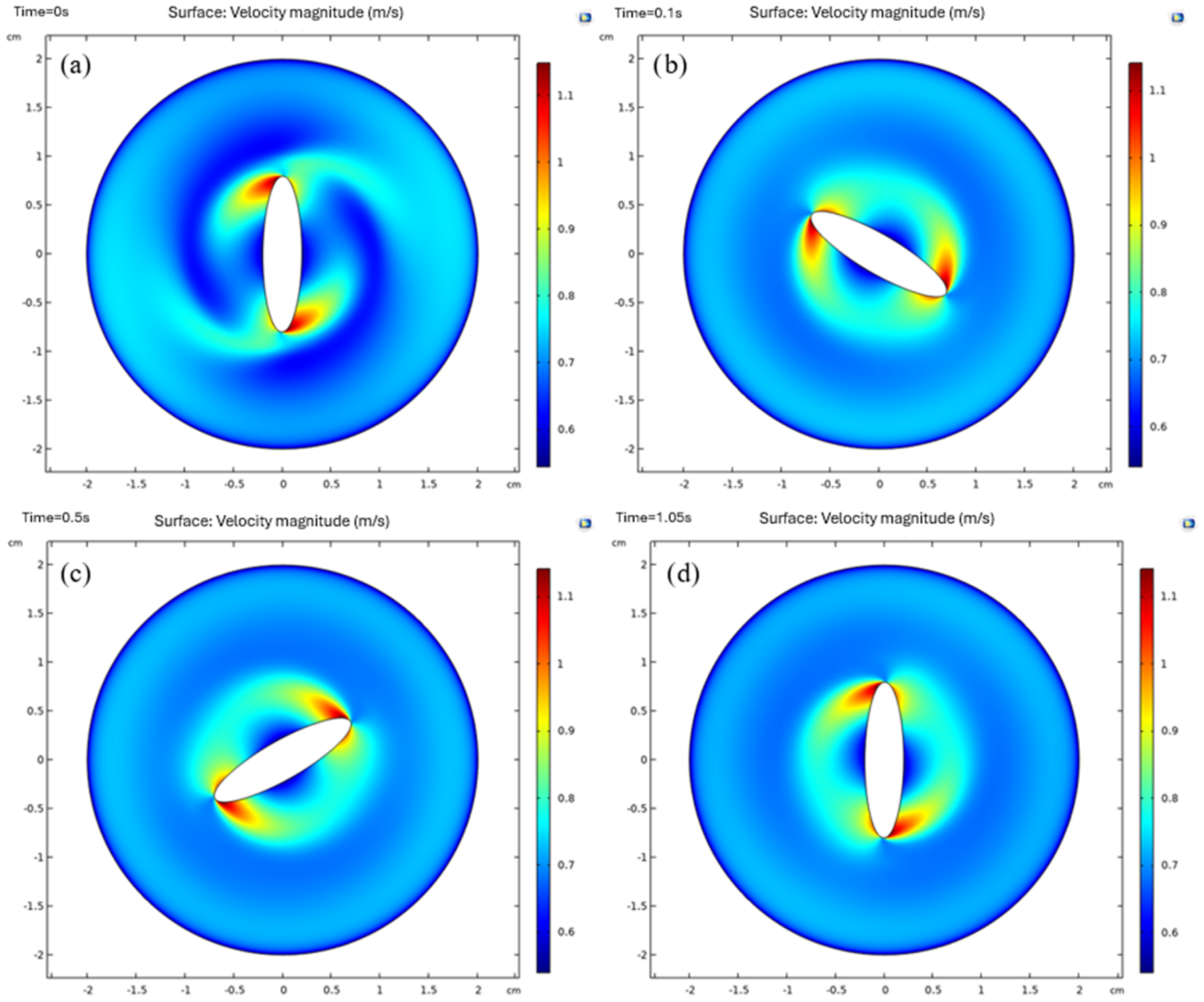

Figure 11. Velocity magnitude (top view of the reactor) at (a) 0 s, (b) 0.1 s, (c) 0.5 s, and (d) 1.05 s at 1400 rpm using an elliptical stirrer.

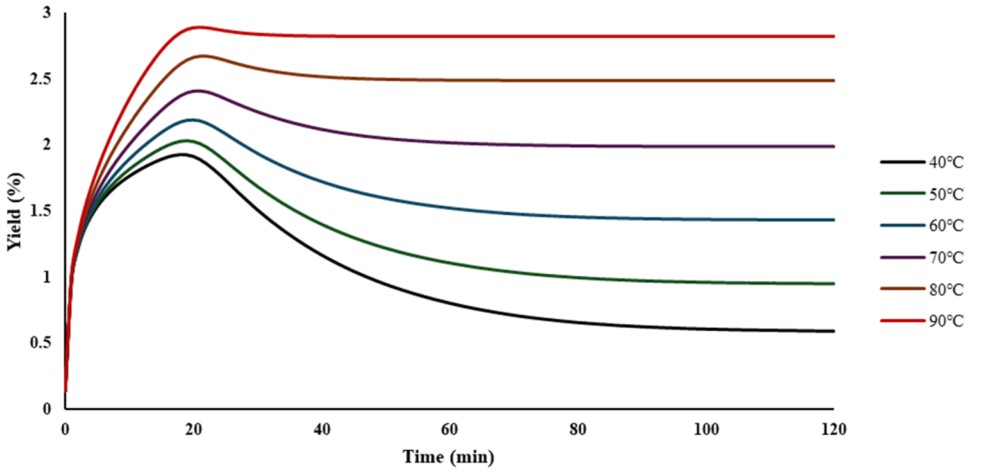

Figure 12. $n(H_2 + N_2)/n(N_2H_4)$ vs time for HH decomposition at temperatures of 40, 50, 60, 70, 80, and 90 °C in a packed-bed microreactor. Simulations conditions: pressure of 1 bar, 0.05 mL/min HH flow, and 9.5 mg of the $Ir/Ni_{10}Ce$ catalyst.

the stirrer within the vessel. The pivot ring stirrer is the original shape of the stirrer used in the experiments. At the beginning (time = 0 s) (Figure 9), the velocity magnitude profile is quite similar to the one achieved with the line stirrer. The velocity field remains unchanged after 0.15 s. It is observed that the velocity magnitude can achieve a lower value near the stirrer

https://doi.org/10.1021/acs.iecr.5c00091
Ind. Eng. Chem. Res. 2025, 64, 8130−8142

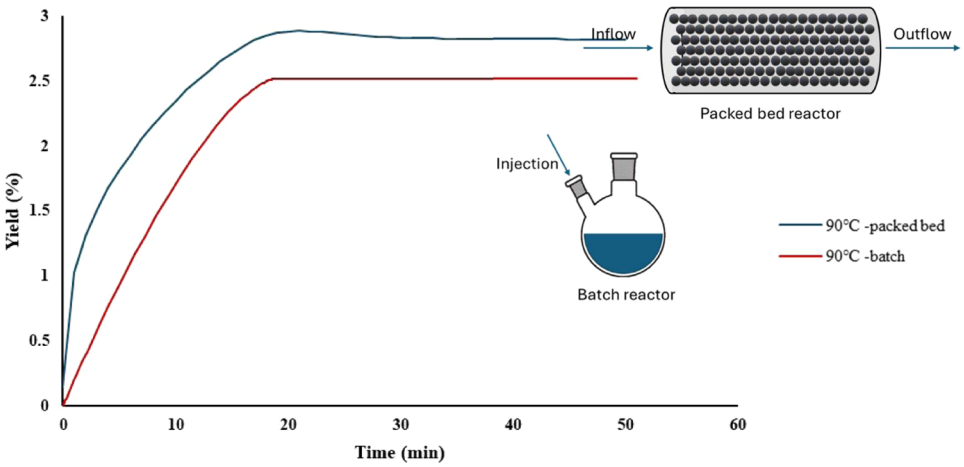

Figure 13. Comparison of batch and packed-bed microreactors at 90 °C. Simulations conditions: Packed-bed microreactor: pressure of 1 bar, 0.05 mL/min HH flow, and 9.5 mg of the Ir/Ni_{10}Ce catalyst. Batch reactor: 1400 rpm, 150 μL of 3.3 M hydrazine monohydrate, and 9.5 mg of the Ir/Ni_{10}Ce catalyst.

(0.2 m/s), and the velocity magnitude is higher at the stirrer's top and bottom. At the rest of the reactor surface area, the values of the velocity magnitude differ slightly compared to the profiles of the line stirrer (0.65 and 0.68 m/s, respectively). However, since it is uniform within the reactor surface, it is confirmed that the reaction is in the kinetic regime.

5.2.2. Cylindrical Stirrer. Cylindrical stirrer bars are very common and have the same shape as the pivot ring stirrers, excluding the ring in the middle. This stirrer was not tested experimentally. It is observed in Figure 10 that the velocity magnitude has a value of 0.67 m/s, similar to the pivot ring stirrer. However, as time passes, it is observed that the area near the stirrer has a higher velocity magnitude than the rest of the surface (0.72 m/s). After 1.65 s, the profile remains the same, with the observation of the development of two zones. This observation can significantly affect the reaction, especially in larger vessels, since it will be limited by diffusion in the area with a lower velocity magnitude.

5.2.3. Elliptical Stirrer. Another available stirrer shape is elliptical, which was not tested experimentally. The velocity magnitude profiles are similar to the cylindrical stirrer (Figure 11). After 1.05 s, the velocity magnitude remains unchanged, and two zones are again observed.

5.2.4. Oval Stirrer. An oval stirrer bar is not so commonly used in such cases. As can be seen from Figure S14, there are no changes in the velocity magnitude over time. Due to the inconvenient shape and size of the stirrer, the mixing is not efficient, achieving only 0.2 m/s of velocity magnitude, which would significantly affect the distribution of both reactant and catalyst particles.

Since the reactor system was simulated on a laboratory scale, it was expected that the influence of the different stirrer shapes would be negligible. However, the oval stirrer was found to be inefficient even for such a small batch system. With such a low velocity magnitude, the reaction will not be kinetically controlled and thus will be limited from external mass transport phenomena. By scaling up the process, the effect of the different stirrer shapes would be more influential on the velocity field and needs to be studied further. It is also noteworthy to mention that the simulations of the stirrer using its original shape and using a line segment did not have significant differences.

5.3. Packed-Bed Microreactor. Continuous flow systems are known to achieve higher yields; however, in the case of HH, continuous flow systems are not usually employed due to the alkali media used in the decomposition reaction, which are corrosive for some materials used in continuous flow systems. Conversely, batch systems have been preferred so far and are also easy to moderate. However, it is interesting to do a comparison study between the two system reactors; thus, a CFD study on a continuous flow system was used. The results are analyzed as explained below and can be used for comparison purposes in future experimental studies.

Figure 12 depicts the normalized ratio over time for a packed-bed microreactor simulated at a temperature range of 40−90 °C. With an increase in the temperature, conversion is increased and thus the yield. Around 20 min into the reaction, the ratio reaches a maximum value at each temperature and then drops, excluding the highest temperature of 90 °C, where it remains almost constant. The drop can be explained by the formation of NH_3, which, in the case of a continuous flow system, might cause deactivation and decreased yield over time.

By comparing the results from the batch system and the packed bed at 90 °C (Figure 13), it is evident that for the same reaction time, the packed bed can achieve better yield results even after a slight drop after 20 min.

6. CONCLUSIONS

Summarizing, this study focuses on the decomposition of hydrous hydrazine to generate hydrogen, highlighting the crucial role of integrating experimental research with CFD simulations. The analysis examined thoroughly how variables such as temperature, stirring rate, mass of catalyst, hydrazine concentration, and NaOH addition influence hydrogen yield and reaction kinetics. Experimental results, supported by CFD studies, determined the best conditions for the reaction decomposition over the developed Ir/Ni_{10}Ce catalyst toward H_2 generation with over 80% yield. Beyond validating the experimental findings, CFD simulations offered an in-depth understanding of the systems' uniformity, particularly focusing on temperature and velocity field distributions. Under these conditions, temperature was distributed uniformly at 30 min, and the profiles of the velocity magnitude were uniform under

https://doi.org/10.1021/acs.iecr.5c00091
Ind. Eng. Chem. Res. 2025, 64, 8130−8142

1 s. Following, different batch geometry and 2D stirrer designs were examined. Even though the batch geometry was slightly different, the velocity magnitude profile was not uniform, with a lower velocity magnitude and dead zones observed near the reactor walls. The 1D and 2D (original shape of the stirrer) stirrers' velocity magnitude profiles were similar in terms of uniformity, highlighting the accuracy of the model. The smallest stirrer modeled resulted in a poor mixing profile, emphasizing the importance of choosing a suitable stirrer, especially when considering scaling up the process. Lastly, a packed-bed microreactor was simulated to compare the batch reactor performance, where the packed bed demonstrated better results in terms of yield toward H_2. However, due to the continuous flow, in addition to H_2, NH_3 was also generated, which resulted in reduced yield. The outcomes of this research make a significant contribution to the integration of experimental and CFD data on hydrous hydrazine decomposition for catalytic hydrogen generation. Future research will focus on exploring different catalyst compositions and support materials to improve efficiency, since even at lower content, Ir metal is expensive due to its scarcity, compared to nonprecious metals. Future prospects also include scaling up of these systems through CFD studies in order to enhance H_2 generation for fuel technologies.

■ ASSOCIATED CONTENT

Data Availability Statement

Data will be made available on request.

Supporting Information

The Supporting Information is available free of charge at https://pubs.acs.org/doi/10.1021/acs.iecr.5c00091.

CFD methodology, XRD−XPS data, catalytic performance data, TOF values, Arrhenius plot, temperature−velocity−concentration distribution plots, stability test, and STEM-HAADF data (PDF)

■ AUTHOR INFORMATION

Corresponding Authors

Alberto Villa − *Dipartimento di Chimica, Università degli Studi di Milano, Milano I-20133, Italy;* orcid.org/0000-0001-8656-6256; Email: alberto.villa@unimi.it

Achilleas Constantinou − *Department of Chemical Engineering, Cyprus University of Technology, Limassol 3036, Cyprus*; Email: a.konstantinou@cut.ac.cy

Authors

Panayiota Adamou − *Department of Chemical Engineering, Cyprus University of Technology, Limassol 3036, Cyprus*

Eleana Harkou − *Department of Chemical Engineering, Cyprus University of Technology, Limassol 3036, Cyprus*

Silvio Bellomi − *Dipartimento di Chimica, Università degli Studi di Milano, Milano I-20133, Italy*

Ilaria Barlocco − *Dipartimento di Chimica, Università degli Studi di Milano, Milano I-20133, Italy;* orcid.org/0000-0002-5568-9648

Juan Josè Delgado − *Departamento de Ciencia de los Materiales, Ingeniería Metalúrgica y Química Inorgánica, Facultad de Ciencias, Universidad de Cádiz, Puerto Real (Cádiz) E-11510, Spain;* orcid.org/0000-0001-7956-1166

Xiaowei Chen − *Departamento de Ciencia de los Materiales, Ingeniería Metalúrgica y Química Inorgánica, Facultad de Ciencias, Universidad de Cádiz, Puerto Real (Cádiz) E-11510, Spain;* orcid.org/0000-0001-6426-5399

Robert Wojcieszak − *Université de Lorraine, CNRS, L2CM UMR 7053, Nancy F-54000, France;* orcid.org/0000-0002-8956-5846

George Manos − *Department of Chemical Engineering, University College London, London WCIE 7JE, U.K.;* orcid.org/0000-0001-8415-1129

Nikolaos Dimitratos − *Department of Industrial Chemistry "Toso Montanari" and Center for Chemical Catalysis-C3, Alma Mater Studiorum University of Bologna, Bologna 40136, Italy;* orcid.org/0000-0002-6620-4335

Complete contact information is available at: https://pubs.acs.org/10.1021/acs.iecr.5c00091

Author Contributions

P.A.: writing the original draft, investigation, methodology, formal analysis, validation, and visualization. E.H.: investigation, formal analysis, and validation. S.B.: investigation, formal analysis, and validation. I.B.: investigation and formal analysis. J.J.D.: investigation, formal analysis, and reviewing and editing the manuscript. X.C.: investigation, formal analysis, and reviewing and editing the manuscript. R.W.: formal analysis and reviewing and editing the manuscript. G.M.: reviewing and editing the manuscript. N.D.: conceptualization and reviewing and editing the manuscript. A.V.: conceptualization, reviewing and editing, and supervision. A.C.: conceptualization, reviewing and editing the manuscript, and supervision.

Notes

The authors declare no competing financial interest.

■ REFERENCES

(1) Niaz, S.; Manzoor, T.; Pandith, A. H. Hydrogen Storage: Materials, Methods and Perspectives. *Renew. Sustain. Energy Rev.* **2015**, *50*, 457−469.

(2) Singh, S. K.; Xu, Q. Complete Conversion of Hydrous Hydrazine to Hydrogen at Room Temperature for Chemical Hydrogen Storage. *J. Am. Chem. Soc.* **2009**, *131* (50), 18032−18033.

(3) Gu, H.; Ran, R.; Zhou, W.; Shao, Z.; Jin, W.; Xu, N.; Ahn, J. Solid-Oxide Fuel Cell Operated on in Situ Catalytic Decomposition Products of Liquid Hydrazine. *J. Power Sources* **2008**, *177* (2), 323−329.

(4) Zhao, B.; Song, J.; Ran, R.; Shao, Z. Catalytic Decomposition of Hydrous Hydrazine to Hydrogen over Oxide Catalysts at Ambient Conditions for PEMFCs. *Int. J. Hydrog. Energy* **2012**, *37* (1), 1133−1139.

(5) He, L.; Huang, Y.; Liu, X. Y.; Li, L.; Wang, A.; Wang, X.; Mou, C.-Y.; Zhang, T. Structural and Catalytic Properties of Supported Ni−Ir Alloy Catalysts for H2 Generation via Hydrous Hydrazine Decomposition. *Appl. Catal. B Environ.* **2014**, *147*, 779−788.

(6) Manukyan, K. V.; Cross, A.; Rouvimov, S.; Miller, J.; Mukasyan, A. S.; Wolf, E. E. Low Temperature Decomposition of Hydrous Hydrazine over FeNi/Cu Nanoparticles. *Appl. Catal. Gen.* **2014**, *476*, 47−53.

(7) Karatas, Y.; Gülcan, M.; Zahmakiran, M. Silica Supported Ternary NiRuPt Alloy Nanoparticles: Highly Efficient Heterogeneous Catalyst for H2 Generation via Selective Decomposition of Hydrous Hydrazine in Alkaline Solution. *Int. J. Hydrog. Energy* **2020**, *45* (51), 27098−27113.

(8) Genç, A. E.; Küçük, H.; Alp, I. O.; Akça, A. Hydrazine Decomposition on Nickel-Embedded Graphene. *Int. J. Hydrog. Energy* **2020**, *45* (58), 33407−33418.

(9) Singh, S. K.; Xu, Q. Bimetallic Nickel-Iridium Nanocatalysts for Hydrogen Generation by Decomposition of Hydrous Hydrazine. *Chem. Commun.* **2010**, *46* (35), 6545−6547.

(10) He, L.; Huang, Y.; Wang, A.; Liu, Y.; Liu, X.; Chen, X.; Delgado, J. J.; Wang, X.; Zhang, T. Surface Modification of Ni/Al2O3 with Pt: Highly Efficient Catalysts for H2 Generation via Selective Decomposition of Hydrous Hydrazine. *J. Catal.* **2013**, *298*, 1−9.
(11) He, L.; Liang, B.; Huang, Y.; Zhang, T. Design Strategies of Highly Selective Nickel Catalysts for H2 Production via Hydrous Hydrazine Decomposition: A Review. *Natl. Sci. Rev.* **2018**, *5* (3), 356−364.
(12) Tang, S.; Zhang, Z.; Xu, L.; Qin, H.; Dong, J.; Lv, Q.; Han, J.; Song, F. Ultrafine Nickel-Rhodium Nanoparticles Anchored on Two-Dimensional Vanadium Carbide for High Performance Hydrous Hydrazine Decomposition at Mild Conditions. *J. Colloid Interface Sci.* **2024**, *669*, 228−235.
(13) Singh, S. K.; Lu, Z.-H.; Xu, Q. Temperature-Induced Enhancement of Catalytic Performance in Selective Hydrogen Generation from Hydrous Hydrazine with Ni-Based Nanocatalysts for Chemical Hydrogen Storage. *Eur. J. Inorg. Chem.* **2011**, *2011* (14), 2232−2237.
(14) Singh, S. K.; Xu, Q. Nanocatalysts for Hydrogen Generation from Hydrazine. *Catal. Sci. Technol.* **2013**, *3* (8), No. 1889.
(15) Zhou, L.; Luo, X.; Xu, L.; Wan, C.; Ye, M. Pt-Ni Nanoalloys for H2 Generation from Hydrous Hydrazine. *Catalysts* **2020**, *10* (8), No. 930.
(16) Jiang, Y.-Y.; Dai, H.-B.; Zhong, Y.-J.; Chen, D.-M.; Wang, P. Complete and Rapid Conversion of Hydrazine Monohydrate to Hydrogen over Supported Ni−Pt Nanoparticles on Mesoporous Ceria for Chemical Hydrogen Storage. *Chem. − Eur. J.* **2015**, *21* (43), 15439−15445.
(17) Singh, S. K.; Zhang, X.-B.; Xu, Q. Room-Temperature Hydrogen Generation from Hydrous Hydrazine for Chemical Hydrogen Storage. *J. Am. Chem. Soc.* **2009**, *131* (29), 9894−9895.
(18) Zhang, P.-X.; Wang, Y.-G.; Huang, Y.-Q.; Zhang, T.; Wu, G.-S.; Li, J. Density Functional Theory Investigations on the Catalytic Mechanisms of Hydrazine Decompositions on Ir(1 1 1). *Catal. Today* **2011**, *165* (1), 80−88.
(19) Lu, X.; Francis, S.; Motta, D.; Dimitratos, N.; Roldan, A. Mechanistic Study of Hydrazine Decomposition on Ir(111). *Phys. Chem. Chem. Phys.* **2020**, *22* (7), 3883−3896.
(20) Bellomi, S.; Motta, D.; Stucchi, M.; Prati, L.; Dimitratos, N.; Villa, A. Hydrogen Production from Hydrous Hydrazine Decomposition Using Ir Catalysts: Effect of the Preparation Method and the Support. *Catalysts* **2024**, *14* (2), No. 119.
(21) Harkou, E.; Hafeez, S.; Adamou, P.; Zhang, Z.; Tsiotsias, A. I.; Charisiou, N. D.; Goula, M. A.; Al-Salem, S. M.; Manos, G.; Constantinou, A. Different Reactor Configurations for Enhancement of CO2Methanation. *Environ. Res.* **2023**, *236*, No. 116760.
(22) Hafeez, S.; Harkou, E.; Adamou, P.; Barlocco, I.; Zanella, E.; Manos, G.; Al-Salem, S. M.; Chen, X.; Delgado, J. J.; Dimitratos, N.; Villa, A.; Constantinou, A. Formic Acid Decomposition Using Palladium-Zinc Preformed Colloidal Nanoparticles Supported on Carbon Nanofibre in Batch and Continuous Flow Reactors: Experimental and Computational Fluid Dynamics Modelling Studies. *Nanomaterials* **2023**, *13* (23), No. 2993.
(23) Harkou, E.; Adamou, P.; Georgiou, K.; Hafeez, S.; Al-Salem, S. M.; Villa, A.; Manos, G.; Dimitratos, N.; Constantinou, A. Computational Studies on Microreactors for the Decomposition of Formic Acid for Hydrogen Production Using Heterogeneous Catalysts. *Molecules* **2023**, *28* (14), No. 5399.
(24) Hafeez, S.; Aristodemou, E.; Manos, G.; Al-Salem, S. M.; Constantinou, A. Computational Fluid Dynamics (CFD) and Reaction Modelling Study of Bio-Oil Catalytic Hydrodeoxygenation in Microreactors. *React. Chem. Eng.* **2020**, *5* (6), 1083−1092.
(25) Chiuta, S.; Everson, R. C.; Neomagus, H. W. J. P.; Bessarabov, D. G. Hydrogen Production from Ammonia Decomposition over a Commercial Ru/Al2O3 Catalyst in a Microchannel Reactor: Experimental Validation and CFD Simulation. *Int. J. Hydrog. Energy* **2016**, *41* (6), 3774−3785.
(26) Shwe Hla, S.; Dolan, M. D. CFD Modelling of a Membrane Reactor for Hydrogen Production from Ammonia. *IOP Conf. Ser. Mater. Sci. Eng.* **2018**, *297* (1), No. 012027.
(27) Maleki, H.; Fulton, M.; Bertola, V. Kinetic Assessment of H2 Production from NH3 Decomposition over CoCeAlO Catalyst in a Microreactor: Experiments and CFD Modelling. *Chem. Eng. J.* **2021**, *411*, No. 128595.
(28) Adamou, P.; Bellomi, S.; Harkou, E.; Chen, X.; Delgado, J. J.; Dimitratos, N.; Manos, G.; Villa, A.; Constantinou, A. Hydrous Hydrazine Decomposition over Rh/Al2O3 Catalyst: Experimental and CFD Studies. *Chem. Eng. J.* **2024**, *493*, No. 152715.
(29) Motta, D.; Barlocco, I.; Bellomi, S.; Villa, A.; Dimitratos, N. Hydrous Hydrazine Decomposition for Hydrogen Production Using of Ir/CeO2: Effect of Reaction Parameters on the Activity. *Nanomaterials* **2021**, *11* (5), No. 1340.
(30) Berčič, G.; Likozar, B. Analysis and Recompilation of Kinetic Data about the Hydrogen Production by the Catalytic Decomposition of Hydrous Hydrazine. *Int. J. Hydrog. Energy* **2022**, *47* (68), 29348−29357.
(31) Bellomi, S.; Cano-Blanco, D. C.; Barlocco, I.; Delgado, J. J.; Chen, X.; Prati, L.; Ferri, D.; Dimitratos, N.; Roldan, A.; Villa, A. Probing the Metal/Oxide Interface of IrCoCeOx in N2H4·H2O Decomposition: An Experimental and Computational Study. *ACS Appl. Mater. Interfaces* **2024**, *16* (40), 54897−54906.
(32) Wang, J.; Li, Y.; Zhang, Y. Precious-Metal-Free Nanocatalysts for Highly Efficient Hydrogen Production from Hydrous Hydrazine. *Adv. Funct. Mater.* **2014**, *24* (45), 7073−7077.
(33) Dai, H.; Zhong, Y.; Wang, P. Hydrogen Generation from Decomposition of Hydrous Hydrazine over Ni-Ir/CeO2 Catalyst. *Prog. Nat. Sci. Mater. Int.* **2017**, *27* (1), 121−125.
(34) Dai, H.; Dai, H.-B.; Zhong, Y.-J.; Kang, Q.; Sun, L.-X.; Wang, P. Kinetics of Catalytic Decomposition of Hydrous Hydrazine over CeO2-Supported Bimetallic Ni−Pt Nanocatalysts. *Int. J. Hydrog. Energy* **2017**, *42* (9), 5684−5693.
(35) Scott, Fogler H. Elements of Chemical Reaction Engineering 5th ed.; 2016.
(36) Wang, J.; Zhang, X.-B.; Wang, Z.-L.; Wang, L.-M.; Zhang, Y. Rhodium−Nickel Nanoparticles Grown on Graphene as Highly Efficient Catalyst for Complete Decomposition of Hydrous Hydrazine at Room Temperature for Chemical Hydrogen Storage. *Energy Environ. Sci.* **2012**, *5* (5), 6885−6888.
(37) He, L.; Huang, Y.; Wang, A.; Wang, X.; Zhang, T. H2 Production by Selective Decomposition of Hydrous Hydrazine over Raney Ni Catalyst under Ambient Conditions. *AIChE J.* **2013**, *59* (11), 4297−4302.
(38) Barlocco, I.; Bellomi, S.; Tumiati, S.; Fumagalli, P.; Dimitratos, N.; Roldan, A.; Villa, A. Selective Decomposition of Hydrazine over Metal Free Carbonaceous Materials. *Phys. Chem. Chem. Phys.* **2022**, *24* (5), 3017−3029.
(39) Zhong, Y.-J.; Dai, H.-B.; Zhu, M.; Wang, P. Catalytic Decomposition of Hydrous Hydrazine over NiPt/La2O3 Catalyst: A High-Performance Hydrogen Storage System. *Int. J. Hydrog. Energy* **2016**, *41* (26), 11042−11049.
(40) Zhang, J.; Kang, Q.; Yang, Z.; Dai, H.; Zhuang, D.; Wang, P. A Cost-Effective NiMoB−La(OH) 3 Catalyst for Hydrogen Generation from Decomposition of Alkaline Hydrous Hydrazine Solution. *J. Mater. Chem. A* **2013**, *1* (38), 11623−11628.

https://doi.org/10.1021/acs.iecr.5c00091
Ind. Eng. Chem. Res. 2025, 64, 8130−8142